Inorganic Chemistry

pubs.acs.org/IC Article

Full Conformational Analyses of the Ultrafast Isomerization in Penta-coordinated $Ru(S_2C_2(CF_3)_2)(CO)(PPh_3)_2$: One Compound, Two Crystal Structures, Three CO Frequencies, 24 Stereoisomers, and 48 Transition States

Hao Tang, Tyler M. Porter, Clifford P. Kubiak, and Michael B. Hall*

Cite This: *Inorg. Chem.* 2020, 59, 11757−11769 Read Online

ACCESS | Metrics & More | Article Recommendations | Supporting Information

ABSTRACT: The stereodynamics of an ultrafast (picosecond) isomerization in a penta-coordinated ruthenium complex, $Ru(S_2C_2(CF_3)_2)(CO)(PPh_3)_2$, were characterized by density functional theory (DFT). The ruthenium complex crystallizes in two almost-square pyramidal (SP) forms. The violet form has an apical PPh_3 ligand, the orange form has an apical CO ligand, and their solution displays three CO stretching frequencies. With 4 possible centers of chirality (1 ruthenium, 2 phosphines, and 1 dithiolate), there are 24 stereoisomers. DFT calculations of these stereoisomers show structures ranging from almost-perfect SP ($\tau_5 \approx 0$) to structures significantly distorted toward trigonal bipyramidal (TBP) ($\tau_5 \approx 0.6$). The stereoisomers fall neatly into three groups, with $\nu_{CO} \approx 1960$ cm^{-1}, 1940 cm^{-1}, and 1980 cm^{-1}. These isomers were found to interconvert over relatively small barriers via Ru−S bond twisting, CF_3 rotation, phenyl twisting, PPh_3 rotation, and, in some cases, by coupled motions. The composite energy surface for each CO frequency group shows that interconversions among the low-energy structures are possible via both the direct and indirect pathways, while the indirect pathway via isomers in the $\nu_{CO} \approx 1980$ cm^{-1} group is more favorable, which is a result consistent with recent experimental work. This work provides the first complete mechanistic picture of the ultrafast isomerization of penta-coordinated, distorted SP, d^6-transition-metal complexes.

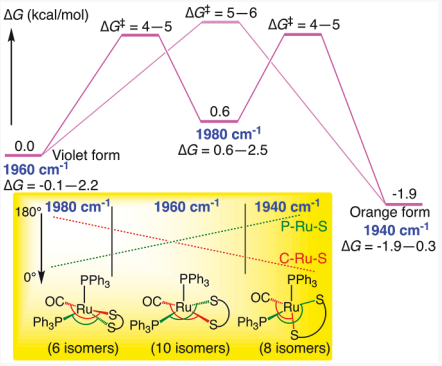

1. INTRODUCTION

The conformational flexibility of penta-coordinated compounds plays a key role in the stereoselectivity and catalytic activity in metallocomplexes.[1−11] Although the interconversions between ideal trigonal bipyramidal (TBP) and ideal square pyramidal (SP) structures of penta-coordinated compounds are usually facile and rapid,[12] alternative nonideal coordination geometries[13−19] and their fluxional behavior[1−7,11b,20−27] present a challenge for simple intramolecular exchange mechanisms. Over the past decades, several mechanistic proposals for different metal−ligand species have been made.[1−7,20b,20,8a,9,13−19,21−38] Berry pseudorotation (BPR)[29] is the most commonly proposed mechanism to describe the interchange of axial and equatorial substituents of penta-coordinated, TBP species. In addition to BPR, other mechanisms include the following: the tetrahedral jump for quasi-tetrahedral HML_4 and H_2ML_3 complexes;[2,20b,38] the turnstile rotation,[20,34−37,39,40] which involves an internal rotation of a *trio*, with respect to *pair* of substituents; and the reverse BPR,[9,17,41] which stereomutates more stable SP structures through a TBP transition state (TS). In addition, three new rearrangement mechanisms—modified Berry pseudorotation, octahedral switch, and butterfly isomerization—have been postulated to account for the nonideal penta-coordinated d^7-transition-metal complexes.[11a] However, very few studies[9,42] address the apical and equatorial ligand exchange in distorted-SP penta-coordinated, d^6-transition-metal complexes.

The penta-coordinated ruthenium complex, $Ru(S_2C_2(CF_3)_2)(CO)(PPh_3)_2$, was first synthesized and characterized by Miller and Balch in 1971, and was found to exist as two different crystalline forms: **1-a** (violet, Figure 1) and **2-c** (orange, Figure 1).[43a] Single-crystal X-ray diffraction (XRD) studies revealed that both conformers had a SP geometry and differed only in the site of the carbonyl ligand. The more-stable orange isomer was found to have the CO ligand in the apical position while the violet isomer had the CO in the equatorial position.[43] Recently, the stereodynamics of this ruthenium complex and related ones have been characterized by using both Fourier transform and two-dimensional (2D) infrared (IR)

Received: June 9, 2020
Published: August 6, 2020

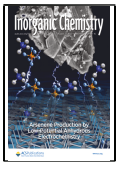

https://dx.doi.org/10.1021/acs.inorgchem.0c01708
Inorg. Chem. 2020, 59, 11757−11769

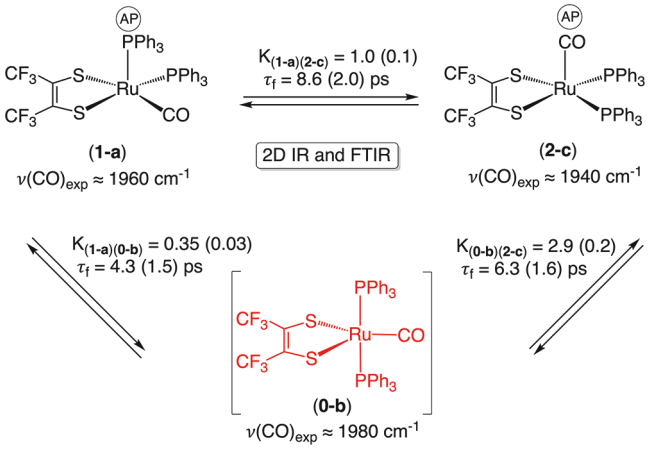

Figure 1. Isomerization of $Ru(S_2C_2(CF_3)_2)(CO)(PPh_3)_2$ as previously described.[44] Although the structure of **0-b** in ChemDraw (above) seems to be TBP with axial PPh_3 groups, their DFT optimized structure for **0-b** is closer to a distorted SP with an apical S, as indicated by the two greatest valence angles (S−Ru−C = 178.1° and P−Ru−P = 163.6°). By comparison of the experimental and DFT computed thermodynamic and kinetic data, this work shows that a different isomer with an apical PPh_3 and a distorted SP geometry (τ_5 = 0.4) is more consistent with the experimentally observed CO frequency near 1980 cm^{-1} (see Figure S1 in the Supporting Information (SI)).

spectroscopy.[44] In dichloromethane solutions, three individual carbonyl stretching frequencies (ν_{CO}) in the vicinity of 1960, 1940, and 1980 cm^{-1} were observed. The ν_{CO} bands near 1940 and 1960 cm^{-1} are in good agreement with the previously reported solid-state Fourier transform infrared (FTIR) spectra[43a] of the orange and violet isomers, respectively. The third ν_{CO} band near 1980 cm^{-1} was classified as a nonisolable, metastable TBP isomer. By using 2D IR spectroscopy, the ultrafast interconversion of the violet ($CO_{equatorial}$, **1-a**) and orange (CO_{apical}, **2-c**) isomers in solution was observed to occur in a few picoseconds ($k \approx 10^{-12}$), and proposed to be mediated by a TBP intermediate (**0-b**), following a reverse BPR mechanism (Figure 1). The experimentally determined thermodynamic stabilities of these isomers from the most stable **2-c** to the least stable **0-b** and the kinetic data for their interchange are shown in Figure 1.

Interestingly, as shown in Scheme 1, the detailed geometries of the isomers reveal that this ruthenium compound has chirality not only at the ruthenium itself (**I**, **II**, **III**), but also on the enantiomeric conformations of metal-coordinated PPh_3 (denoted as $\mathbf{P_M}$ and $\mathbf{P_P}$),[45] and of the $S_2C_2(CF_3)_2$ group (denoted as $\mathbf{L_U}$ and $\mathbf{L_D}$). These conformational features of the $S_2C_2(CF_3)_2$ group have been observed in the crystal structures, where the CF_3 groups were experimentally observed to have large librational motion[43c,d] and disorder.[44b] Specifically, the crystallographically determined equatorial CO isomer **1**, which is structurally denoted as $\mathbf{1}(\mathbf{I}^{\mathbf{P_PP_M}}_{\mathbf{L_U}})$, has Ru in the **I** conformation, the equatorial PPh_3 in the $\mathbf{P_M}$ conformation, the apical PPh_3 in the $\mathbf{P_P}$ conformation, and the CF_3 groups in the $\mathbf{L_U}$ conformation. In contrast, the crystallographically determined apical CO isomer **5′**, which is denoted as $\mathbf{5'}(\mathbf{II}^{\mathbf{P_PP_M}}_{\mathbf{L_D}})$ has Ru in the **II** conformation, the equatorial PPh_3 groups in $\mathbf{P_P}$ and $\mathbf{P_M}$ conformations, and the CF_3 groups in the $\mathbf{L_D}$ conformation.

Based on the assumption that transition states connecting the different stereoisomers involve changes of one stereocenter at a time, possible stereomutation mechanisms of this penta-coordinated ruthenium species are displayed in Scheme 2. For the ruthenium stereochemistry, twisting either of the Ru−S bonds from a basal site of the SP to the vacant octahedral position lead to the apical and basal ligand interchange, producing three conformations (**I**, **II**, and **III**). The enantiomeric conformations **I** and **III** bear the apical PPh_3 in the SP structure, whereas conformation **II** possess the apical CO in the SP structure (Scheme 2a). This stereomutation resembles both the octahedral switch mechanism described by Asatryan, Ruckenstein, and Hachmann for penta-coordinated d^7 $HM(CO)_4$ complexes,[11a] and the equatorial−axial ligand exchange mechanism involving a C_{2V} TS proposed by Burdett et al. for penta-coordinated d^6 $M(CO)_5$ complexes.[9] Exchange between the $\mathbf{L_U}$ and $\mathbf{L_D}$ conformations of the CF_3 group occurs via CF_3 group rotation (Scheme 2b), while the metal coordinated PPh_3 conformations of $\mathbf{P_M}$ and $\mathbf{P_P}$ are interchanged through the phenyl rings twisting (Scheme 2c). It is possible for a PPh_3 ligand to remain in the same conformation while simply rotating about the Ru−P bond. This effectively changes the orientation of the phenyl ring, with respect to the other ligands (Scheme 2d).

Taking these permutations into account, for the violet, $CO_{equatorial}$ isomer, chirality about the ruthenium (**I** and **III**), the phosphine ligands (**M** and **P**), and dithiolate ligand (**U** and **D**), results in four stereochemical centers, giving 16 stereoisomers and 8 diastereomers. Furthermore, the orange CO_{apical} isomer,

Scheme 1. Possible Stereogenic Centers for (a) Ru (I, II, and III), (b) PPh_3 (P_P and P_M), and (c) $S_2C_2(CF_3)_2$ Group (L_U and L_D), and (d) the Two Crystal Structures[a]

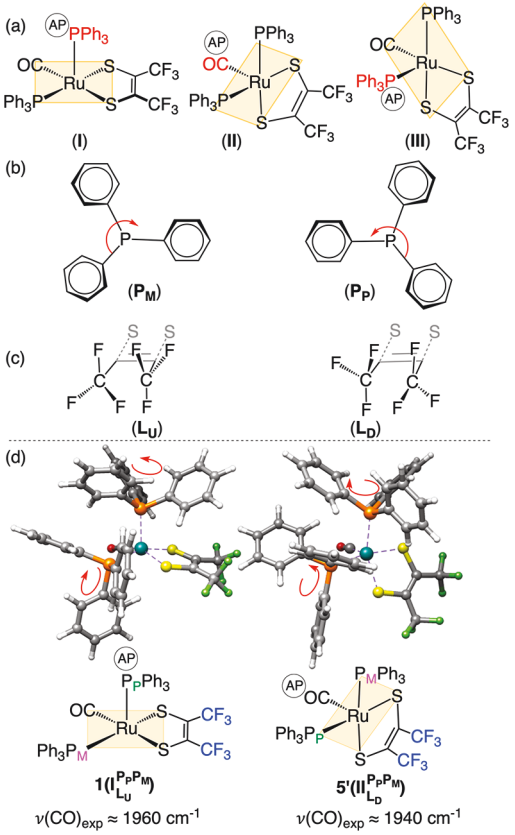

[a] $\mathbf{P_M}$ indicates that the phenyl rings are clockwise on the phosphorus, while $\mathbf{P_P}$ indicates that the phenyl rings are counterclockwise on the phosphorus.

https://dx.doi.org/10.1021/acs.inorgchem.0c01708
Inorg. Chem. 2020, 59, 11757−11769

Scheme 2. Possible General Stereomutation Mechanisms

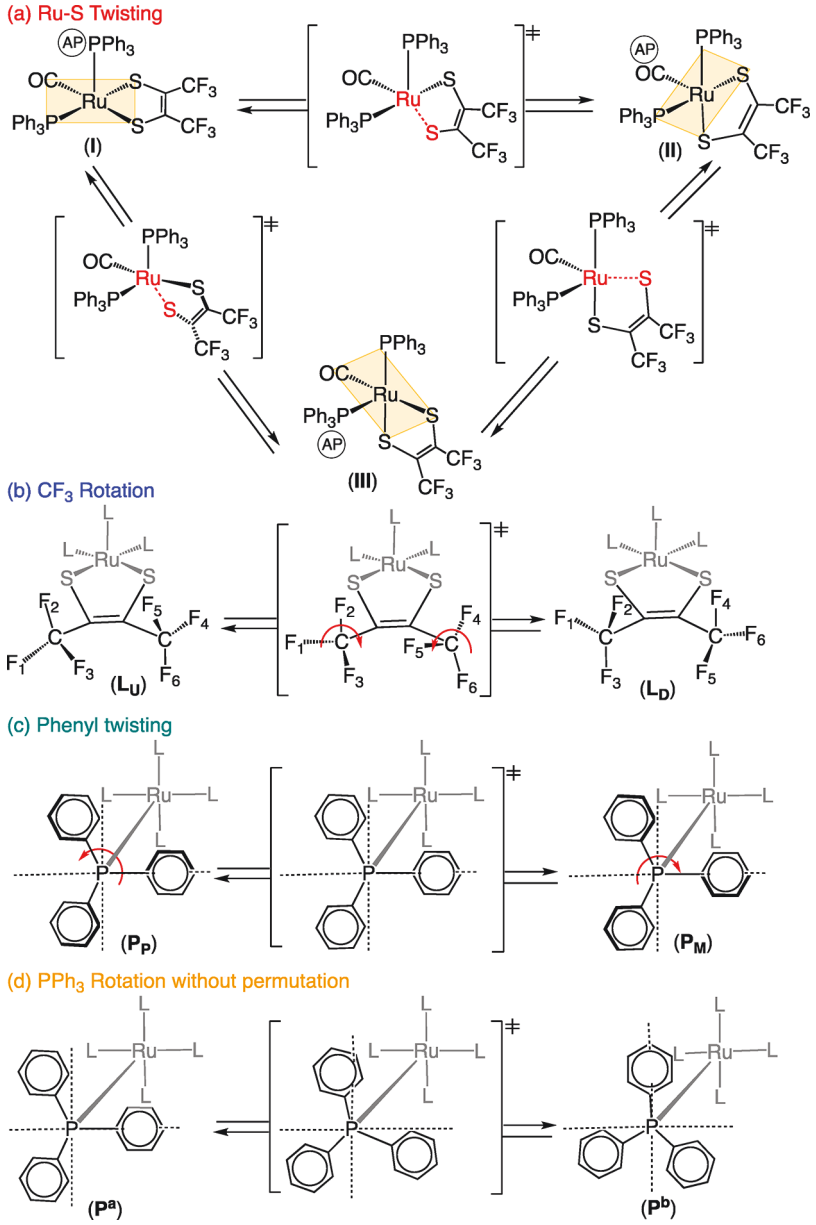

II, has three stereochemical centers, resulting in 8 stereoisomers and 4 diastereomers. Thus, this system has 12 diastereomers in total, each with different energies and spectral signatures; however, if the barriers for the PPh_3 rotation (Scheme 2d) are large enough, there could be even more. The possibility of such a large number of diastereomers raises a number of crucial questions:

(1) What isomeric transformation(s) connect the two crystallographically characterized systems?
(2) What paths connect these to the metastable third isomer?
(3) Do the three experimentally observed ν_{CO} bands near 1960, 1940, and 1980 cm^{-1} correspond to single diastereoisomers or do several related diastereomers have similar energies and frequencies?
(4) Could alternative diastereomers be stabilized under other solvo-thermo conditions?
(5) Are there more isomers of these compounds that correspond to other ligand arrangements?

In this paper, by beginning with each crystal structure, all of the possible stereomutation mechanisms (Scheme 2) were examined with DFT calculations. Each subsequently formed stereoisomer was then transformed by all possible paths until all the interchange pathways and stereoisomers were found. The resulting stereoisomers, conformational isomerization mechanisms, and the critical points, including transition states, on the potential energy surfaces were comprehensively analyzed. Furthermore, we assigned the three, experimentally observed, ν_{CO} bands (~1960, 1940, and 1980 cm^{-1}) into three groups of diastereoisomers. This detailed mechanistic study provides a complete picture of the conformational isomerization in a penta-coordinated, d^6-transition-metal complex.

2. COMPUTATIONAL METHODS

DFT calculations were performed with the Gaussian 09 program suite.[46] Benchmarking studies with six different DFT functionals, including BP86,[47,48] TPSS,[49] ω-B97XD,[50] B3LYP,[47,48a,b] B3P86,[47,48c] and M06[51,52] are shown in the Supporting Information (SI).

https://dx.doi.org/10.1021/acs.inorgchem.0c01708
Inorg. Chem. 2020, 59, 11757−11769

Comparisons of the energies and geometries of the singlet and triplet states for optimized geometries corresponding to **1** and **5′** show that (i) the singlet states are significantly more stable and (ii) their geometries are more consistent with experimental data, compared to the corresponding higher-energy TBP-like triplet states (Tables S1−S3 in the SI). Thus, we only focus on the singlet states for all of the isomers.

The geometries of **1** and **5′** were sensitive to DFT functionals, dispersion corrections, and implicit solvation corrections (see Tables S4−S8 in the SI). Specifically, the BP86, TPSS, B3P86, and B3LYP functionals reproduce the experimental geometries of **1** and **5′** much better than ω-B97XD, M06, and BP86 with empirical dispersion corrections (BP86-GD3BJ),[53] especially for **5′**, where the dispersion correction increases the C−Ru−S2 angle and decreases the P2−Ru−S2 angle (Scheme 3 and Table S6). Reoptimizing the geometries of **1** and **5′** in solvent with BP86, BP86-GD3BJ, B3P86, M06, and ω-B97XD functionals (Tables S5, S7, and S8) decreases the C−Ru−S2 angle and increases the P2−Ru−S2 angle (Scheme 3 and Table S7).

Scheme 3. Two Key Angles in 5′: C−Ru−S2 and P2−Ru−S2

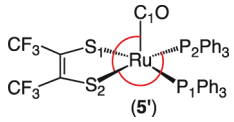

Therefore, all of the geometries were fully optimized without symmetry constraints in the gas-phase using the BP86 functional in combination with the basis set def2-TZVP[54] (Ru, S, P, and O) and def2-SVP[54] (C and H) (denoted as BS1). By comparison with the larger basis set def2-TZVP for all the atoms (denoted as BS2), BS1 was found to be an acceptable compromise between accuracy and cost (see Tables S4−S7 and S9 in the SI, and Schemes S1 and S2 in the SI). Harmonic vibrational frequency analysis was calculated at the same level to confirm the nature of the minima (no imaginary frequency) and transition states (only one imaginary frequency). The thermal corrections, entropy terms, and the CO frequencies for the optimized geometries were obtained from the frequency calculations. The transition states were verified to connect reactants and products through intrinsic reaction coordinate (IRC)[55] calculations.

Single-point calculations were computed at these gas-phase optimized structures with the BP86/def2-TZVPP[56] (denoted as BS3) level of theory. Solvation effects using methylene chloride (DCM) as the solvent were taken into account in the single point calculations with the continuum solvation model SMD.[57] DFT-D3 with BJ damping empirical dispersion corrections was employed for the BP86 functional in the single-point calculations. All of the reported energies and barriers in this work include BS2 gas-phase thermal correction at 298.15 K. To facilitate the comparison, the experimental barriers were transformed to $\Delta H^{\ddagger}$ values, using the relation $\Delta H^{\ddagger} = E_a - RT$, where E_a is the activation energy, R the gas constant, and T the temperature.

To distinguish the degree of distortion in an isomer's geometry, the parameter τ_5, ranging from SP ($\tau_5 = 0$) to TBP ($\tau_5 = 1$), as proposed by Addison et al.,[58] is reported (Scheme 4).

Scheme 4. Ideal Square Pyramidal and Trigonal Bipyramidal Geometries[a]

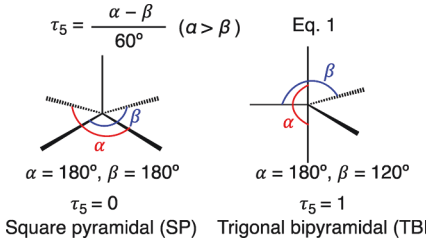

[a]α and β are the two greatest valence angles (ligand−M−ligand). A value of $\tau_5 = 0$ indicates an ideal SP, while a value of $\tau_5 = 1$ indicates an ideal TBP.

3. RESULTS AND DISCUSSION

Scheme 5 shows the 24 possible stereoisomers on the basis of four chiral centers: ruthenium (**I**, **II** and **III**), each P ($\mathbf{P_P}$ and $\mathbf{P_M}$), and the two CF_3 groups ($\mathbf{L_U}$ and $\mathbf{L_D}$), and the stereomutations that convert one to another. Unexpectedly, isomers $\mathbf{13}(\mathbf{II}^{P_MP_P}_{L_U})/\mathbf{13'}(\mathbf{II}^{P_MP_P}_{L_D})$ and $\mathbf{14}(\mathbf{I}^{P_MP_P}_{L_U})/\mathbf{14'}(\mathbf{I}^{P_MP_P}_{L_D})$ (the P in the first order denotes the apical PPh_3 conformation) are not transformed to the expected low-energy isomers from their respective Ru stereochemistry (**I**, **II**, **III**) via twisting one of the Ru−S bonds (Scheme 5 in blue; see Figure S2 in the SI). Specifically, isomers **13**/**13′** are high in energy (4.5 kcal/mol), because of the steric hindrance of the two phenyl rings at two phosphines (Figure S2). The twist permutation of the dithiolate ligand in either $\mathbf{5}(\mathbf{II}^{P_PP_M}_{L_U})/\mathbf{5'}(\mathbf{II}^{P_PP_M}_{L_D})$ or $\mathbf{10}(\mathbf{III}^{P_PP_M}_{L_U})/\mathbf{10'}(\mathbf{III}^{P_PP_M}_{L_D})$ is expected to produce the corresponding isomers $\mathbf{14}(\mathbf{I}^{P_MP_P}_{L_U})/\mathbf{14'}(\mathbf{II}^{P_MP_P}_{L_D})$. However, the calculations predict that the transition state reconnects the isomers **5**/**5′** and **10**/**10′** without passing through **14**/**14′**, likely because of the high thermodynamic stability of **5**/**5′**. Although **14**/**14′** can be found (Figure S2), the conversion from **14**/**14′** to **5**/**5′** appears to be almost barrierless, so **14**/**14′** was not included as stable species in the rearrangement scheme. This result also holds true for the other tested DFT functionals, such as B3LYP, TPSS, and B3P86. The alternative isomers $\mathbf{3}(\mathbf{I}^{P^a_MP_M}_{L_U})/\mathbf{3'}(\mathbf{I}^{P^a_MP_M}_{L_D})$ and $\mathbf{9}(\mathbf{III}^{P^b_MP_P}_{L_U})/\mathbf{9'}(\mathbf{III}^{P^b_MP_P}_{L_D})$ (where superscripts a and b indicate of the phenyl rings positional changes without permutation) are involved in the rearrangement scheme.

Scheme 5. 24 Stereoisomers in This System[a]

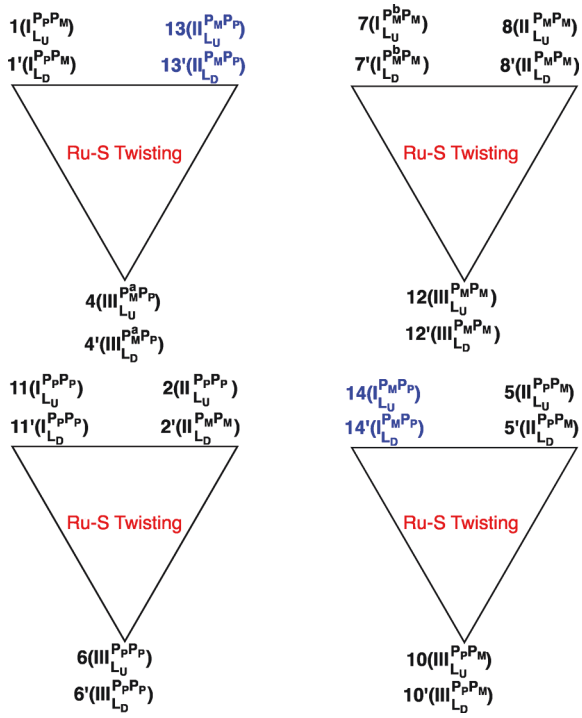

[a]The isomers $\mathbf{13}(\mathbf{II}^{P_MP_P}_{L_U})/\mathbf{13'}(\mathbf{II}^{P_MP_P}_{L_D})$ and $\mathbf{14}(\mathbf{I}^{P_MP_P}_{L_U})/\mathbf{14'}(\mathbf{I}^{P_MP_P}_{L_D})$ (Figure S2) are not involved in the rearrangement scheme (see below).

https://dx.doi.org/10.1021/acs.inorgchem.0c01708
Inorg. Chem. 2020, 59, 11757−11769

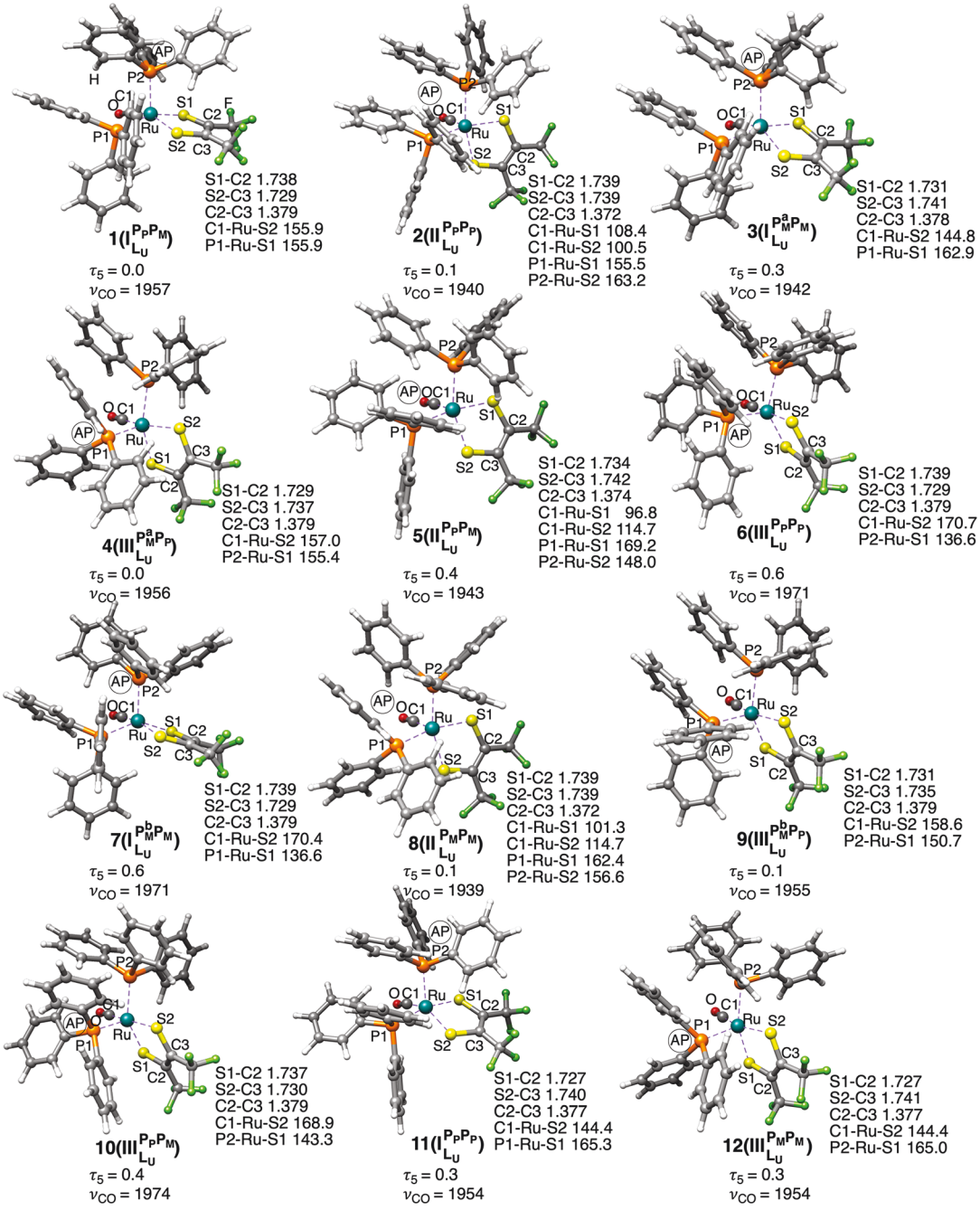

Figure 2. DFT-optimized geometries of stereoisomers **1**−**12** with selected bond distances (Å) and angles (deg), the parameter τ_5, and scaled CO frequencies (cm^{-1}) at the BP86/BS2 level. The scaling factor for ν_{CO} is obtained by averaging the two individual scaling factors of two crystals **1** and **5′**. "AP" in the circle denotes the apical position in the SP structure, which is displayed in the first order in the notation, while superscripts "a" and "b" indicate PPh_3 rotation without Ph twisting.

Figure 2 depicts the diastereoisomers **1**−**12** with the CF_3 group conformation $\mathbf{L_U}$, and their enantiomers **1′**−**12′** with the CF_3 group conformation $\mathbf{L_D}$ are given in Scheme S3. Inspection of the computed τ_5 values (0.0−0.6) in Figure 2 reveals that all isomers have the distorted geometries, wherein isomers **1**−**5**, **8**−**12** are displaced toward SP structures (τ_5 = 0.0−0.4), while isomer **6** and **7** feature a more TBP-like structure (τ_5 = 0.6). Similar to the crystal structure of the violet isomer, **1**($I^{P_PP_M}_{L_U}$) isomers **3**($I^{P^a_MP_M}_{L_U}$), **7**($I^{P^b_MP_M}_{L_U}$), and **11**($I^{P_PP_P}_{L_U}$) bear the ruthenium stereochemistry **I** with an equatorial CO, while isomers **2**($II^{P_PP_P}_{L_U}$), **5**($II^{P_PP_M}_{L_U}$), and **8**($II^{P_MP_M}_{L_U}$) resemble the orange isomer, which is **5′**($II^{P_PP_M}_{L_D}$) with an apical CO and ruthenium stereochemistry **II**. Isomers **4**($III^{P^a_MP_P}_{L_U}$), **6**($III^{P_PP_P}_{L_U}$), **9**($III^{P^b_MP_P}_{L_U}$), **10**($III^{P_PP_M}_{L_U}$), and **12**($III^{P_MP_M}_{L_U}$) have an equatorial CO with the alternative ruthenium stereochemistry **III**. The calculated average C−C and C−S bond distances for all the isomers (**1**−**12**) of 1.377 and 1.735 Å, respectively (Figure 2), are in good accord with the dithiolate (two electron-reduced) character of the ligand (C−C and C−S bond distances of 1.337 and 1.761 Å),[59] which yields a Ru(II) d^6 assignment for all the isomers **1**−**12**, in excellent agreement with the experiment.[44]

https://dx.doi.org/10.1021/acs.inorgchem.0c01708
Inorg. Chem. 2020, 59, 11757−11769

Comparisons of isomers **1**−**12** (Figure 2) and the corresponding isomers **1′**−**12′** (Scheme S3) indicate that the CF_3 group conformational interchange between $\mathbf{L_U}$ and $\mathbf{L_D}$ has little influence on the geometries, relative free energies, and CO frequencies. The small Gibbs free-energy barriers (<2.3 kcal/mol) indicate that the interconversion between isomers **1**−**12** and the corresponding isomer **1′**−**12′** occur easily and fast at room temperature, which is supported by experimental work on the crystal structures[43c,d] and the related ruthenium complexes.[44b] To simplify our presentation, we focus on the isomers **1**−**12** with the CF_3 group conformation $\mathbf{L_U}$ in the main text, similar details about the isomers **1′**−**12′** with the CF_3 group conformation $\mathbf{L_D}$ are displayed in the SI.

In a previous study, three ν_{CO} bands near 1980, 1960, and 1940 cm^{-1} were observed in solution.[44] DFT calculations show that the scaled ν_{CO} frequencies for isomers **1** (1957 cm^{-1}), **4** (1956 cm^{-1}), **9** (1955 cm^{-1}), **11** (1954 cm^{-1}), and **12** (1954 cm^{-1}) are in good agreement with the experimentally observed ν_{CO} band at 1960 cm^{-1}, as are the scaled ν_{CO} frequencies for isomers **2** (1940 cm^{-1}), **3** (1942 cm^{-1}), **5** (1943 cm^{-1}), and **8** (1939 cm^{-1}) with the reported ν_{CO} band near 1940 cm^{-1}. The third ν_{CO} band in the vicinity of 1980 cm^{-1} was found to correspond well with isomers **6** (1971 cm^{-1}), **7** (1971 cm^{-1}), and **10** (1974 cm^{-1}). To elucidate if the DFT functional and basis set would cause any significant ν_{CO} changes in isomers, the geometries of **1**−**12** were reoptimized in gas phase with B3P86, TPSS, and B3LYP functionals in combination with the larger basis set BS2. The resulting scaled ν_{CO} values of **1**−**12** match those obtained at BP86/BS1 and BP86/BS2 levels very well (see Table S9 in the SI).

Unexpectedly, for isomers **1**−**12**, there is not a clear connection between CO position, frequency, or Ru stereochemistry (**I**, **II**, and **III**). However, inspection of other geometric parameters for all the isomers (except **3**) reveals that two valence angles (θ_1 = C−Ru−S and θ_2 = P−Ru−S) exhibit a clear trend, relative to the CO frequency spanning 1980 cm^{-1} to 1940 cm^{-1} (Figure 3). The orange isomer with $\nu_{CO} \approx$ 1940 cm^{-1} corresponds to **5**/**5′** with ν_{CO} = 1943 cm^{-1}, the violet isomer with $\nu_{CO} \approx$ 1960 cm^{-1} corresponds to **1** with ν_{CO} = 1957 cm^{-1}, and the spectroscopically characterized isomer with $\nu_{CO} \approx$ 1980 cm^{-1} corresponds to isomer **10** with ν_{CO} = 1972 cm^{-1}. In Figure 3, one can follow the changes of the key angles (θ_1 = C−Ru−S and θ_2 = P−Ru−S) from **10** (168.9°, 143.3°) to **1** (155.9°, 155.9°) and finally to **5** (114.7°, 169.2°).

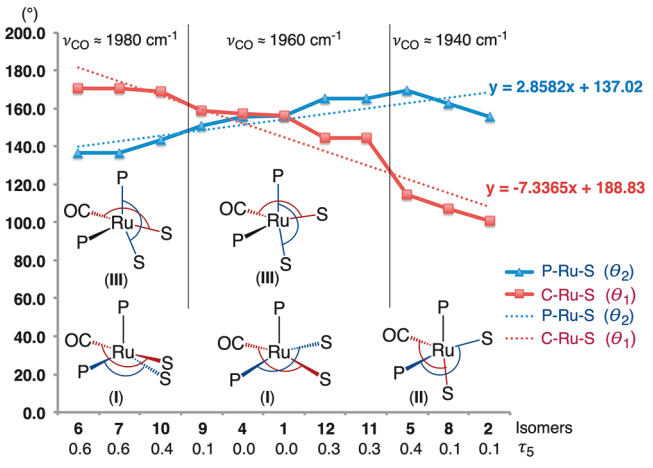

Figure 3. Correlation of the CO frequencies with the two valence angles (θ_1 and θ_2) of the isomers (**1**, **2**, **4**−**12**). θ_1 and θ_2 are the two greatest valence angles in Ru (**I** and **III**). θ_1 = C−Ru−S2 and θ_2 = P1−Ru−S1 in **I**, θ_1 = C−Ru−S2 and θ_2 = P2−Ru−S1 in **III**, and θ_1 = C−Ru−S2 and θ_2 = P1−Ru−S1 in **II** in Figure 2.

Isomer **3**($\mathbf{I}_{\mathbf{L_U}}^{\mathbf{P_M^a P_M}}$) presents a special case. Although **3** has geometric parameters like isomer **11**($\mathbf{I}_{\mathbf{L_U}}^{\mathbf{P_P P_P}}$)(Figure 4), as

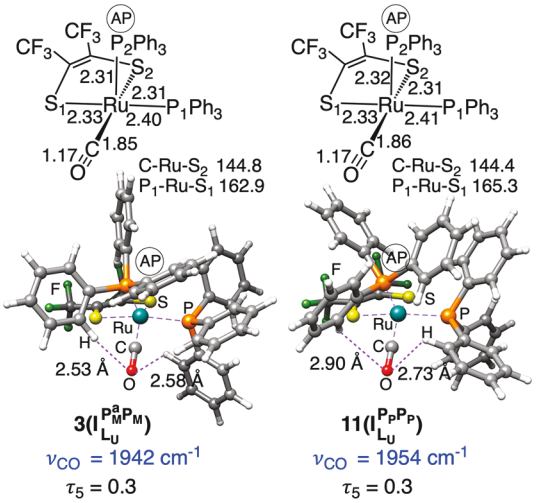

Figure 4. Comparisons of key geometric parameters (bond distances are given in Å, and angles are given in degrees), hydrogen bond distances, and CO frequencies between isomers **3** and **11**.

reflected by the Ru−S, Ru−P, Ru−C distances and especially the key angles of θ_1 and θ_2 (144.8° and 162.9° for **3**, 144.4° and 165.3° for **11**), the CO frequencies for isomer **3** (1942 cm^{-1}) and **11** (1954 cm^{-1}) are in different ranges, near 1940 and 1960 cm^{-1}, respectively. The similar geometries but different CO frequencies can be explained by the formation of a hydrogen bond (H−O) between the H in the phenyl ring and the O in carbonyl ligand, H−O. Figure 4 shows that the $\mathbf{P_M}$ conformations of both PPh_3 in isomer **3** render shorter H−O bond distances of 2.53 and 2.58 Å, while the $\mathbf{P_P}$ conformations of both PPh_3 in isomer **11** render longer H−O bond distances of 2.90 and 2.73 Å. The stronger H−O bonds in isomer **3** decrease the CO frequency by withdrawing electron density, such as weak carbonyl−cation interactions.[60]

To better understand the relationship between thermodynamic stability and CO frequency for isomers **1**−**12**, the isomers were divided into three subsets relating their DFT calculated ν_{CO} frequencies (Scheme 6). The first subset consists of isomers **1**, **4**, **9**, **11**, and **12** with ν_{CO} frequencies near 1960 cm^{-1} and are ranked in order of decreasing stability as (**4**, **1**) > (**12**, **11**) > (**9**). The second subset contains isomers **2**, **3**, **5**, and **8** with a υ_{CO} frequency near 1940 cm^{-1} and a relative stability ranking of (**5**) > (**3**) > (**2**, **8**). Finally, the third subset corresponds to isomers **6**, **7**, and **10** with υ_{CO} frequencies near 1980 cm^{-1} and are ranked with relative stabilities of (**10**) > (**6**, **7**). Upon comparing the most stable isomers for each subset, the thermodynamic stability was found to decrease from **5**, to **1** and **4**, and further to **10**. This thermodynamic order holds true for all tested DFT functionals with a larger basis set (Scheme S1 in the SI) and is completely consistent with the experimental results.[44]

To assess the isomerization pathways shown in Scheme 6, both those connecting isomers belonging to one CO frequency group and those that cause the shift to another frequency group, we examined all the possible interchange pathways (Scheme 2)

https://dx.doi.org/10.1021/acs.inorgchem.0c01708
Inorg. Chem. 2020, 59, 11757−11769

Scheme 6. Relative Free Energies (ΔG) of the Isomers 1−12 (Small Circles) and the Free-Energy Barriers ($\Delta G^{\ddagger}$) for All the Possible Interchange Pathways among the Isomers Grouped (Large Ovals), According to Their CO Frequencies near 1980, 1960, and 1940 cm^{-1} at the BP86-GD3BJ(SMD)/BS3//BP86/BS2 Level[a]

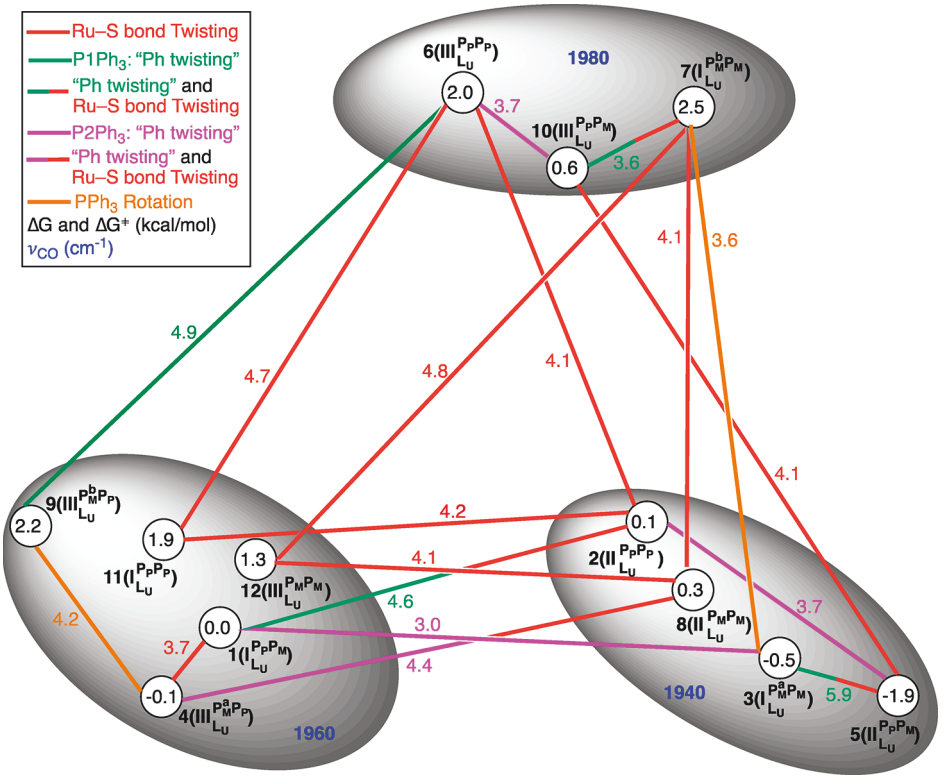

[a]The vermilion lines indicate interchange of the Ru stereochemistry (**I**, **II**, **III**) by twisting either of the Ru−S bonds. The bluish green and magenta lines indicate permutations of the conformation of two respective $P1Ph_3$ and $P2Ph_3$ (see Figure 2 for the definitions of $P1Ph_3$ and $P2Ph_3$) between $\mathbf{P_M}$ and $\mathbf{P_P}$ via Ph twisting. The lines in two colors indicate coupling of Ph twisting with the proximal Ru−S bond twisting. The orange lines indicate a change in the PPh_3 position by rotation about the Ru−P bond without stereomutation. All the energies and barriers are relative to that of isomer **1**.

for transition states connecting the species until all the corresponding 24 stereoisomers and 48 transition states were found. The full stereoisomerization mechanism with the free-energy data is given in Scheme S3 in the SI. To simplify, only isomers **1**−**12** ($\mathbf{L_U}$ isomers) are shown in Scheme 6, where the critical points on the potential energy surfaces (PESs) for each isomer and interchange pathway are arranged in groups according to their CO frequencies. There is a similar trend for the $\mathbf{L_D}$ isomers and the barriers between $\mathbf{L_U}$ and $\mathbf{L_D}$ isomers are low and independent of the other pathways (see Scheme S3).

As shown in Scheme 6, beginning with the violet isomer, **1** ($\mathbf{I}^{\mathbf{P_PP_M}}_{\mathbf{L_U}}$) ($\nu_{CO}$ = 1957 cm^{-1}), three pathways are available. The first pathway involves twisting one of the Ru−S bonds in **1** yielding **13**($\mathbf{II}^{\mathbf{P_MP_P}}_{\mathbf{L_U}}$) (Scheme 5). However, this twisting was found to be coupled to stereomutation of the equatorial PPh_3 ligand, inverting the conformation from $\mathbf{P_M}$ to $\mathbf{P_P}$ coincident with interconversion the Ru stereochemistry from **I** to **II**. This ultimately yields the slightly less stable (0.1 kcal/mol) isomer **2**($\mathbf{II}^{\mathbf{P_PP_P}}_{\mathbf{L_U}}$) ($\nu_{CO}$ = 1940 cm^{-1}) by traversing a 4.6 kcal/mol barrier. However, twisting the other Ru−S bond in **1** produces a TBP-like transition structure ($\mathbf{TS_{1-4}}$, τ_5 = 0.7) with the barrier of 3.7 kcal/mol, forming the slightly more stable (−0.1 kcal/mol) isomer **4**($\mathbf{III}^{\mathbf{P^a_MP_P}}_{\mathbf{L_U}}$) ($\nu_{CO}$ = 1956 cm^{-1}). A third pathway involving conformational interchange of the apical PPh_3 in **1** from $\mathbf{P_P}$ to $\mathbf{P_M}$ was also observed and found to have a low barrier of 3.0 kcal/mol. This conformational interchange produces the slightly more stable (−0.5 kcal/mol) isomer **3**($\mathbf{I}^{\mathbf{P^a_MP_M}}_{\mathbf{L_U}}$) ($\nu_{CO}$ = 1942 cm^{-1}).

As observed in the description above for **1**, **4**($\mathbf{III}^{\mathbf{P^a_MP_P}}_{\mathbf{L_U}}$) was also found to have a coupled stereomutation of the equatorial PPh_3 from $\mathbf{P_P}$ to $\mathbf{P_M}$, which simultaneously interconverts the Ru stereochemistry from **III** to **II** as well. This coupled mutation was found to have a 4.5 kcal/mol barrier and produce the slightly less stable (by 0.4 kcal/mol) isomer **8**($\mathbf{II}^{\mathbf{P_MP_M}}_{\mathbf{L_U}}$) ($\nu_{CO}$ = 1939 cm^{-1}). While a simple twist of the dithiolate ligand in **4**($\mathbf{III}^{\mathbf{P^a_MP_P}}_{\mathbf{L_U}}$) would also be expected to yield **13**($\mathbf{II}^{\mathbf{P_MP_P}}_{\mathbf{L_U}}$), this mechanism however is not observed and instead follows the coupled pathway. In addition, however, **4**($\mathbf{III}^{\mathbf{P^a_MP_P}}_{\mathbf{L_U}}$) could generate the less stable (by 2.3 kcal/mol) isomer **9**($\mathbf{III}^{\mathbf{P^b_MP_P}}_{\mathbf{L_U}}$) ($\nu_{CO}$ = 1955 cm^{-1}) by rotation of the apical PPh_3 wherein only the position of apical phosphine changes while the conformation ($\mathbf{P_M}$) is retained. This was found to have a 4.3 kcal/mol barrier. A rotation is observed for the interconversion of **3**($\mathbf{I}^{\mathbf{P^a_MP_M}}_{\mathbf{L_U}}$) ($\nu_{CO}$ = 1942 cm^{-1}) and **7**($\mathbf{I}^{\mathbf{P^b_MP_M}}_{\mathbf{L_U}}$) ($\nu_{CO}$ = 1971 cm^{-1}).

The most stable isomer, **5**($\mathbf{II}^{\mathbf{P_PP_M}}_{\mathbf{L_U}}$) ($\nu_{CO}$ = 1943 cm^{-1}, the $\mathbf{L_U}$ form of the orange CO_{apical} crystal), was easily generated from **2**($\mathbf{II}^{\mathbf{P_PP_P}}_{\mathbf{L_U}}$) ($\nu_{CO}$ = 1940 cm^{-1}) by permutation of the equatorial

https://dx.doi.org/10.1021/acs.inorgchem.0c01708
Inorg. Chem. 2020, 59, 11757−11769

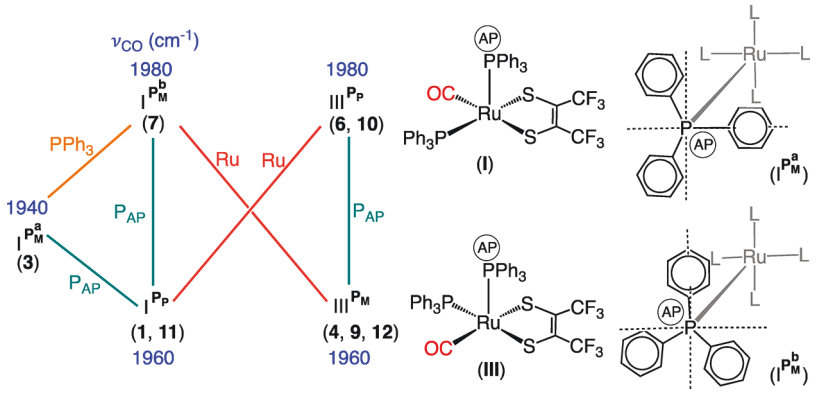

Figure 5. Correlation of the CO frequencies with the ruthenium stereochemistry (**I** and **III**), the apical PPh_3 conformation ($\mathbf{P_M}$ and $\mathbf{P_P}$), and the apical PPh_3 position ($\mathbf{P^a}$ and $\mathbf{P^b}$) of the equatorial CO structures.

PPh_3 from conformation $\mathbf{P_P}$ to $\mathbf{P_M}$, as reflected by the small of 3.6 kcal/mol barrier. Alternatively, while isomer **5**($\mathbf{II}_{L_U}^{P_PP_M}$) could be expected to form **14**($\mathbf{I}_{L_U}^{P_MP_P}$) (Scheme 5) by a dithiolate twist, it instead follows a coupled pathway to form the less stable (by 1.4 kcal/mol) isomer **3**($\mathbf{I}_{L_U}^{P^a_MP_M}$) ($\nu_{CO}$ = 1942 cm^{-1}). The coupled pathway is similar to those described above where the equatorial PPh_3 conformation from **3** to **5** is inverted from $\mathbf{P_M}$ to $\mathbf{P_P}$ coincident with a dithiolate twist. Lastly, **5** was also found to be formed from **10**($\mathbf{III}_{L_U}^{P_PP_M}$) ($\nu_{CO}$ = 1974 cm^{-1}) by a 3.5 kcal/mol barrier through an uncoupled dithiolate twist.

While an alternative twist of the dithiolate ligand in **10**($\mathbf{III}_{L_U}^{P_PP_M}$) can form **14**($\mathbf{I}_{L_U}^{P_MP_P}$) (Scheme 5), the calculations predict that the twist is coupled to stereomutation of the apical PPh_3 inverting its stereochemistry from $\mathbf{P_P}$ to $\mathbf{P_M}$. This mutation was found to produce the less stable (by 1.9 kcal/mol) isomer **7**($\mathbf{I}_{L_U}^{P^b_MP_M}$) ($\nu_{CO}$ = 1971 cm^{-1}) by traversing a 3.0 kcal/mol barrier. Isomer **10**($\mathbf{III}_{L_U}^{P_PP_M}$) was additionally found to yield the less stable (by 1.4 kcal/mol) isomer **6**($\mathbf{III}_{L_U}^{P_PP_P}$) ($\nu_{CO}$ = 1971 cm^{-1}) by interchange of the equatorial PPh_3 conformation from $\mathbf{P_M}$ to $\mathbf{P_P}$ with a 3.1 kcal/mol barrier. Furthermore, interconversion between **6**($\mathbf{III}_{L_U}^{P_PP_P}$) and **9**($\mathbf{III}_{L_U}^{P^b_MP_P}$) was also found to have an ~3 kcal/mol barrier and occurs by conformation change of the apical PPh_3 between $\mathbf{P_M}$ and $\mathbf{P_P}$.

Although twisting of the Ru−S bond is sometimes coupled to permutation of phosphine configuration, there were several cases where it is uncoupled. One such example involves the interconversion among isomers **2**($\mathbf{II}_{L_U}^{P_PP_P}$) ($\nu_{CO}$ = 1940 cm^{-1}), **6**($\mathbf{III}_{L_U}^{P_PP_P}$) ($\nu_{CO}$ = 1971 cm^{-1}), and **11**($\mathbf{I}_{L_U}^{P_PP_P}$) ($\nu_{CO}$ = 1954 cm^{-1}), where a simple dithiolate twist about the Ru−S bond was found to have barriers of only 2−4 kcal/mol. Similarly, isomers **7**($\mathbf{I}_{L_U}^{P^b_MP_M}$) ($\nu_{CO}$ = 1971 cm^{-1}), **8**($\mathbf{II}_{L_U}^{P_MP_M}$) ($\nu_{CO}$ = 1939 cm^{-1}), and **12**($\mathbf{III}_{L_U}^{P_MP_M}$) ($\nu_{CO}$ = 1954 cm^{-1}) can also undergo a similar transformation with similar barriers.

Generally, all the interchange pathways require such small barriers (<8 kcal/mol), that exchange among the stereoisomers with the ν_{CO} near 1960, 1940, and 1980 cm^{-1} are expected to occur rapidly at room temperature. These findings are in excellent agreement with experimental observations.[44]

Surprisingly, the three CO frequencies arise from only two stereochemistries at Ru, since all the species in Scheme 6 have either an apical CO or an equatorial CO. The equatorial CO structures can vary their CO frequencies by as much as 40 cm^{-1} through simple distortions of the phosphine ligands. This phenomenon involves changes of the apical PPh_3 conformation, as shown in Figure 5. Specifically, when the ruthenium stereochemistry remains the same, changing the apical PPh_3 conformation from $\mathbf{P_M}$ to $\mathbf{P_P}$ affects their CO frequencies by 20 cm^{-1} (bluish green lines in Figure 5), but changing both generates their enantiomers. Thus, isomers with $\mathbf{I}^{P_M}$($\mathbf{III}^{P_P}$) have ν_{CO} near 1980 cm^{-1} while the isomers with $\mathbf{I}^{P_P}$($\mathbf{III}^{P_M}$) have ν_{CO} near 1960 cm^{-1}. Similarly, when the apical PPh_3 conformation remains the same, changing the ruthenium stereochemistry affects their CO frequencies by 20 wavenumbers (vermilion lines in Figure 5). Even more striking is the change from isomer **7**($\mathbf{I}_{L_U}^{P^b_MP_M}$) ($\nu_{CO}$ ≈ 1980 cm^{-1}) to **3**($\mathbf{I}_{L_U}^{P^a_MP_M}$) ($\nu_{CO}$ ≈ 1940 cm^{-1}), which affects their CO frequencies by ~40 cm^{-1} through simple PPh_3 rotation without permutation (orange line in Figure 5).

The apical PPh_3 conformation combined with the Ru stereochemistry controls the (C−Ru−S) angle, which has the major influence on the CO frequencies (Figure 3). As shown in Figure 6, as the C−Ru−S angle decreases in type **I** species from **7** to **1** and **11**, and finally to type **II** species like **5**, **8**, and **2**, the antibonding interactions between the occupied Ru 4d orbitals and S 3p lone pairs increase, which strengthens the Ru-CO π-backdonation, and thus decreases the CO frequencies, dropping from 1980, to 1960, and to 1940 cm^{-1}. This connection between the CO frequencies and interaction of occupied Ru 4d orbitals and S 3p lone pairs is also responsible for the fact that isomers with $\mathbf{III}^{P_P}$ (**6**, **10**) have ν_{CO} near 1980 cm^{-1} while the isomers with $\mathbf{III}^{P_M}$ (**4**, **9**, **12**) have ν_{CO} near 1960 cm^{-1}. In addition, the stronger H−OC interaction in isomer **3** causes an additional decrease in its CO frequency by strengthening this CO's backbonding as compared to isomer **11** that has a similar geometry (i.e., C−Ru−S angle) but a weaker H−OC interaction and a higher CO frequency (Figure 4).

Figure 7 shows a composite energy "surface" for the $Ru(S_2C_2(CF_3)_2)(CO)(PPh_3)_2$ isomerization on the basis of the most stable isomers in each CO frequency pattern and the most favorable pathways between each of the most stable isomers. By comparing the thermodynamic stability for each ν_{CO} frequency pattern, the equilibrium is predicted to be dominated by only a few isoenergetic diastereomers and their optical isomers at each CO frequency: 1960 cm^{-1} (**1**, **1′**, **4**, **4′**), 1940 cm^{-1} (**5**, **5′**), 1980 cm^{-1} (**10**, **10′**). Two of these isomers, **1** and **5′**, correspond to the isolable and previously reported crystal structures.[44a] Upon cooling, the experimental spectra showed

https://dx.doi.org/10.1021/acs.inorgchem.0c01708
Inorg. Chem. 2020, 59, 11757−11769

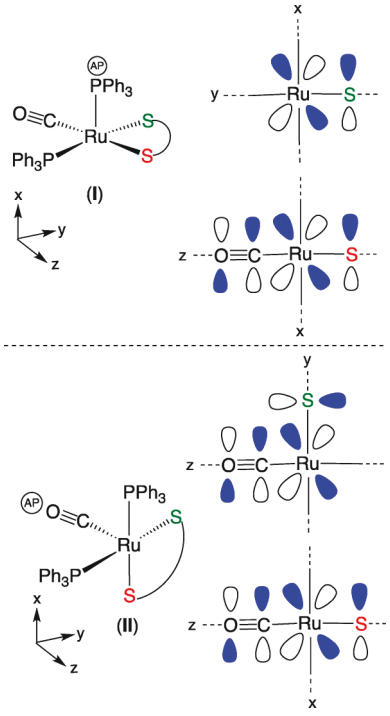

Figure 6. Interactions between occupied Ru 4d and S 3p lone pairs that affect the Ru-CO π-backbonding, and how these change as a function of the valence angle (C−Ru−S) for the isomerization from **I** to **II** (there is a related change for **III** to **II**).

that the 1940 cm^{-1} band sharpens and gains intensity while the shoulders near 1960 and 1980 cm^{-1} significantly lose intensity.[44a] In agreement with the experimental results, the calculations predict that the species at 1940 cm^{-1} (**5**, **5′**) are most stable, while those at 1960 cm^{-1} (**1**, **1′**, **4**, **4′**) are less stable by ΔH(cal) = 2.4, 2.1 kcal/mol (ΔH(exp) = 1.3 kcal/mol) and those at 1980 cm^{-1} (**10**, **10′**) are less stable by ΔH(cal) = 2.2 kcal/mol (ΔH(exp) = 2.18 kcal/mol).

DFT calculations agree with the experimental proposal[44a] that the kinetically favored isomerization between **1-a** (1960 cm^{-1} (**1**, **1′**, **4**, **4′**)) to **2-c** (1940 cm^{-1} (**5**, **5′**)) was indirect by passing through **0-b** (1980 cm^{-1} (**10**, **10′**)) as an intermediate with barriers of $\Delta H_{(1\text{-a})(0\text{-b})}^{\ddagger}$(cal) vs $\Delta H_{(1\text{-a})(0\text{-b})}^{\ddagger}$(exp) = 2.1, 2.4 kcal/mol vs 1.62 kcal/mol and $\Delta H_{(0\text{-b})(2\text{-c})}^{\ddagger}$ (cal) vs $\Delta H_{(0\text{-b})(2\text{-c})}^{\ddagger}$(exp) = 1.5, 1.6 vs 1.82 kcal/mol. However, the calculations show that this path is more complicated as the route from (**1**, **1′**, **4**, **4′**) to (**10**, **10′**) is not direct and must pass through isomers (**3**, **3′**) and (**7**, **7′**) and the route from (**10**, **10′**) to (**5**, **5′**) may proceed directly or through isomers (**2**, **2′**) and (**6**, **6′**) at the same rate. Thus, these other intermediates may have transient existence. In particular, isomers (**2**, **2′**) and (**3**, **3′**) with $\nu_{CO} \approx$ 1940 cm^{-1}, similar to the final product (**5**, **5′**), are almost isoenergetic with isomers (**1**, **1′**, **4**, **4′**), while isomers (**6**, **6′**) and (**7**, **7′**) with $\nu_{CO} \approx$ 1980 cm^{-1}, similar to (**10**, **10′**), are less stable than this intermediate by ~2 kcal/mol. Furthermore, the direct isomerization from (**1**, **1′**, **4**, **4′**) to (**5**, **5′**), which must also pass through isomer (**2**, **2′**), is predicted to be 0.8 kcal/mol lower in enthalpy and only 1.0 kcal/mol higher in free energy. Overall, the enthalpy barriers ($\Delta H^{\ddagger}$) shown in Figure 7 (1.3−

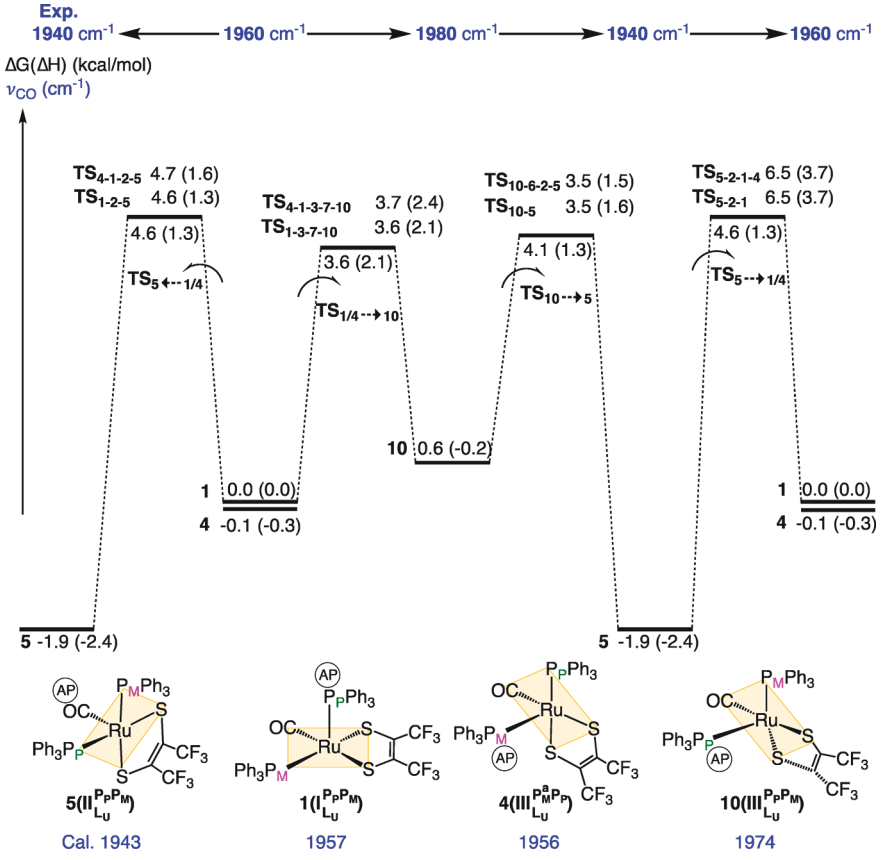

Figure 7. Overall energy profile of the $Ru(S_2C_2(CF_3)_2)(CO)(PPh_3)_2$ isomerization based on the most stable $\mathbf{L_U}$ isomers in each CO frequency pattern ($\nu_{CO} \approx$ 1960 cm^{-1} (**1** and **4**), 1940 cm^{-1} (**5**), and 1980 cm^{-1} (**10**)) at the BP86-GD3BJ(SMD)/BS3//BP86/BS2 level. The vertical energy scale refers to **1** as zero point. The overall barriers in each path refer to their starting isomer, and the details are given in Figure S3 in the SI.

https://dx.doi.org/10.1021/acs.inorgchem.0c01708
Inorg. Chem. 2020, 59, 11757−11769

2.1 kcal/mol) are in good agreement with the experimental ones (1.6−2.0 kcal/mol). These thermodynamic and kinetic trends hold true for the other tested DFT functionals like B3LYP and TPSS (see Figures S4 and S5 in the SI).

Interestingly, upon close inspection of the experimental 2D IR spectra, the diagonal peak intensity for **0-b** (1980 cm^{-1}) can be found to recover more slowly, compared to the diagonal peak for **1-a** (1960 cm^{-1}) and **2-c** (1940 cm^{-1}).[44a] In accord with experiment, this observation is supported by the calculated barriers as interchange from **10**/**10′** to **1** (**4**)/**1′** (**4′**) and **5**/**5′** has lower barriers, with respect to other interconversion.

4. CONCLUSION

In summary, this work describes the first detailed computational study of the ultrafast isomerization for the penta-coordinated d^6 ruthenium complex, $Ru(S_2C_2(CF_3)_2)(CO)(P(Ph)_3)_2$. The complex was found to have four chiral centers: one about the ruthenium atom, two about the metal-coordinated phosphine ligands, and one about the dithiolate ligand. DFT calculations were found to predict an astonishing 24 low-energy stereoisomers that are connected by 48 transition states, which were all found by careful examination of all possible interchange pathways (see Scheme 2).

These low-energy isomers were found to have geometries that range from almost square pyramidal to distorted trigonal bipyramidal (τ_5 = 0.0−0.6) and could be divided into three centered about the experimentally observed ν_{CO} frequencies near 1960 cm^{-1} (**1**, **4**, **9**, **11**, **12**), 1940 cm^{-1} (**2**, **3**, **5**, **8**), and 1980 cm^{-1} (**6**, **7**, **10**) and their corresponding L_D isomers. There is a clear connection between the CO frequency and the geometric parameters (θ_1 = C−Ru−S and θ_2 = P−Ru−S) for all the isomers (except **3**, whose ν_{CO} was affected by a C−H···OC hydrogen bond). Strikingly, the equatorial CO structures can vary their CO frequencies by 40 wavenumbers through simple distortions of the phosphine ligands.

While it was not possible to determine the complexity of the isomerization mechanism from the experimental work,[44] since the mechanism involves several low barrier stereomutations: Ru−S bond twisting, CF_3 rotation, phenyl twisting, PPh_3 rotation, and coupled counterparts invoking two mutations at once. Note that the apical and basal ligand interchange occurs via twisting either of the Ru−S bonds from a basal site of the SP to the vacant octahedral position (see Scheme 2a), similar to that observed for the octahedral switch mechanism.[11a] This mechanism has been postulated in an early study,[9] in which the equatorial-axial exchange mechanism was considered to be equivalent to the reverse Berry pseudorotation, and therefore is difficult to distinguish in experiment.[9]

These isomers were shown to interconvert readily at room temperature, as indicated by both experiment and the computed barriers (<8 kcal/mol). By comparing the thermodynamic stability for each ν_{CO} frequency pattern, the equilibrium was found to be dominated by only a few isoenergetic isomers at each CO frequency: 1960 cm^{-1} (**1**, **1′**, **4**, **4′**), 1940 cm^{-1} (**5**, **5′**), 1980 cm^{-1} (**10**, **10′**). Two of these isomers, **1** and **5′**, were found to correspond to the isolable and previously reported crystal structures.[44a] In addition to the most rapid conversions (from **1**−**12** to **1′**−**12′**), the calculations predict that the interconversion between the two most stable forms at 1960 cm^{-1} (**1**, **4**) and 1940 cm^{-1} (**5**) are possible via both direct and indirect pathways, while the indirect pathway via isomer **10** is slightly favored. These barriers are in accord with the experimental work and the 2D IR analysis.[44a]

This work provides detailed insight into the mechanism for the ultrafast isomerization in the penta-coordinated, distorted SP, d^6-transition-metal complex, which may lead to ways to control and test these transformations.

■ ASSOCIATED CONTENT

Supporting Information

The Supporting Information is available free of charge at https://pubs.acs.org/doi/10.1021/acs.inorgchem.0c01708.

Benchmarking with different DFT functionals using BS1 and BS2 basis sets on relative free energies at the low and high spin states, geometric structures optimized in gas and solvent phases, and CO frequencies of **1** and **5′**; relative enthalpy energies of isomers **1**−**12** at DFT/BS2 levels; comparisons of **10** and **0-b**; optimized geometries of isomers **13** and **14**; overall stereomutation mechanisms; PESs for the possible interchange pathways between the isomers with the CO frequencies near 1960 and 1940 cm^{-1}, 1960 and 1980 cm^{-1}, and 1980 and 1940 cm^{-1}; optimized geometries of 24 isomers, and 48 transition states for all the interchange pathways; Cartesian coordinates, and absolute energies (PDF)

■ AUTHOR INFORMATION

Corresponding Author

Michael B. Hall − *Department of Chemistry, Texas A&M University, College Station, Texas 77845, United States;* orcid.org/0000-0003-3263-3219; Email: mbhall@tamu.edu

Authors

Hao Tang − *Department of Chemistry, Texas A&M University, College Station, Texas 77845, United States;* orcid.org/0000-0003-0323-0349

Tyler M. Porter − *Department of Chemistry and Biochemistry, University of California San Diego, La Jolla, California 92093-0358, United States*

Clifford P. Kubiak − *Department of Chemistry and Biochemistry, University of California San Diego, La Jolla, California 92093-0358, United States;* orcid.org/0000-0003-2186-488X

Complete contact information is available at: https://pubs.acs.org/10.1021/acs.inorgchem.0c01708

Author Contributions

All authors have given approval to the final version of the manuscript.

Notes

The authors declare no competing financial interest.

■ ACKNOWLEDGMENTS

We acknowledge financial support from The Welch Foundation (Grant No. A-0648) and the National Science Foundation (Grant No. CHE-1664866). Computer time was provided by the TAMU HPRC Facility and software was provided by the Laboratory for Molecular Simulation. C.P.K. acknowledges support from the National Science Foundation (Grant No. CHE-1853908).

■ REFERENCES

(1) Cotton, F. A. Fluxional organometallic molecules. *Acc. Chem. Res.* **1968**, *1*, 257−265.

(2) Muetterties, E. Stereochemically nonrigid structures. *Acc. Chem. Res.* **1970**, *3*, 266−273.
(3) Hoffmann, R. Building Bridges Between Inorganic and Organic Chemistry (Nobel Lecture). *Angew. Chem., Int. Ed. Engl.* **1982**, *21*, 711−724.
(4) Burdett, J. K. Ligand site preferences and intramolecular photochemical rearrangements in some transition metal complexes. Simple molecular orbital considerations. *Inorg. Chem.* **1976**, *15*, 212−219.
(5) der Heyde, T. A. Determination of Reaction Paths for Pentacoordinate Metal Complexes with the Structure Correlation Method. *Angew. Chem., Int. Ed. Engl.* **1994**, *33*, 823−839.
(6) Dashevskii, V. G.; Asatryan, R.; Baranov, A. P. Interligand interaction and the three-dimensional structure of coordination compounds. monodentate ligands. *J. Struct. Chem.* **1978**, *19*, 404−411.
(7) Gusev, D. G.; Berke, H. Hydride Fluxionality in Transiton Metal Complexes: An Approach to the Understanding of Mechanistic Features and Structural Diversities. *Chem. Ber.* **1996**, *129*, 1143−1155.
(8) (a) Burdett, J. K. *Molecular Shapes: Theoretical Models of Inorganic Stereochemistry*; Wiley: New York, 1980. (b) Pearson, R. G. Symmetry rule for predicting molecular structures. *J. Am. Chem. Soc.* **1969**, *91*, 4947−4955.
(9) Burdett, J. K.; Grzybowski, J. M.; Perutz, R. N.; Poliakoff, M.; Turner, J. J.; Turner, R. F. Photolysis and spectroscopy with polarized light: key to the photochemistry of pentacarbonylchromium and related species. *Inorg. Chem.* **1978**, *17*, 147−154.
(10) Asatryan, R.; Ruckenstein, E. Mechanism of Iron Carbonyl-Catalyzed Hydrogenation of Ethylene. 1. Theoretical Exploration of Molecular Pathways. *J. Phys. Chem. A* **2013**, *117*, 10912−10932.
(11) (a) Asatryan, R.; Ruckenstein, E.; Hachmann, J. Revisiting the polytopal rearrangements in pentacoordinate d^7 metallocomplexes: modified Berry pseudorotation, octahedral switch, and butterfly isomerization. *Chem. Sci.* **2017**, *8*, 5512−5525. (b) Rzepa, H. S.; Cass, M. E. A computational study of the nondissociative mechanisms that interchange apical and equatorial atoms in square pyramidal molecules. *Inorg. Chem.* **2006**, *45*, 3958−3963.
(12) (a) Gillespie, R. J. The stereochemistry of five-co-ordination. Part I. Non-transition elements. *J. Chem. Soc.* **1963**, 4672−4678. (b) Holmes, R. R. Spectroscopy and structure of pentacoordinated molecules. *Acc. Chem. Res.* **1972**, *5*, 296−303.
(13) Ward, T. R.; Bürgi, H.-B.; Gilardoni, F.; Weber, J. Edge-Bridged Tetrahedral Geometry of Five-Coordinate d^0 Complexes, Relatives of the Bent $[MC^{b2}L_3]$ Family: A Theoretical and Structure-Correlation Study. *J. Am. Chem. Soc.* **1997**, *119*, 11974−11985.
(14) Riehl, J.-F.; Jean, Y.; Eisenstein, O.; Pelissier, M. Theoretical study of the structures of electron-deficient d^6 ML_5 complexes. Importance of a π-donating ligand. *Organometallics* **1992**, *11*, 729−737.
(15) Hauger, B. E.; Gusev, D.; Caulton, K. G. Hydrogen binding to and fluxional behavior of $Ir(H)_2X(P^tBu_2R)_2$ (X = = Cl, Br, I; R = = Me, Ph). *J. Am. Chem. Soc.* **1994**, *116*, 208−214.
(16) García-Monforte, M. A.; Baya, M.; Betoré, M. P.; Martín, A.; Menjón, B. Mononuclear anionic AO_2X_3 compounds with non-VSEPR structure. *Dalton Trans.* **2014**, *43*, 7615−7621.
(17) Alvarez, S.; Llunell, M. Continuous symmetry measures of penta-coordinate molecules: Berry and non-Berry distortions of the trigonal bipyramid. *J. Chem. Soc., Dalton Trans.* **2000**, 3288−3303.
(18) Jordan, R. B. *Reaction Mechanisms of Inorganic and Organometallic Systems*; Oxford University Press, 2007; Chapter 4, pp 114−148.
(19) Roddick, D. M.; Zargarian, D. Pentacoordination for pincer and related terdentate coordination compounds: Revisiting structural properties and trends for d^8 transitionmetal systems. *Inorg. Chim. Acta* **2014**, *422*, 251−264.
(20) (a) Moss, G. P. Basic Terminology of Stereochemistry (IUPAC Recommendations 1996). *Pure Appl. Chem.* **1996**, *68*, 2193−2222. (b) Meakin, P.; Muetterties, E. L.; Jesson, J. P. Intramolecular rearrangement mechanisms in five-coordinate complexes. *J. Am. Chem. Soc.* **1972**, *94*, 5271−5285.
(21) Albright, T. A.; Burdett, J. K.; Whangbo, M.-H. *Orbital Interactions in Chemistry*, 2nd Edition; Wiley−Interscience: Hoboken, NJ, 2013; p 834.
(22) Elian, M.; Hoffmann, R. Bonding capabilities of transition metal carbonyl fragments. *Inorg. Chem.* **1975**, *14*, 1058−1076.
(23) Rossi, A. R.; Hoffmann, R. Transition metal pentacoordination. *Inorg. Chem.* **1975**, *14*, 365−374.
(24) Holmes, R. R. Pentacoordinated molecules. 53. Influence of d-orbital occupancy on the geometry of pentacoordinated molecules. *J. Am. Chem. Soc.* **1984**, *106*, 3745−3750.
(25) Church, S. P.; Poliakoff, M.; Timney, J. A.; Turner, J. J. Photochemistry of matrix-isolated $HMn(CO)_5$: evidence for two isomers of $HMn(CO)_4$. *Inorg. Chem.* **1983**, *22*, 3259−3266.
(26) Couzijn, E. P. A.; Slootweg, J. C.; Ehlers, A. W.; Lammertsma, K. Stereomutation of pentavalent compounds: validating the Berry pseudorotation, redressing Ugi's turnstile rotation, and revealing the two- and three-arm turnstiles. *J. Am. Chem. Soc.* **2010**, *132*, 18127−18140.
(27) (a) Muetterties, E. Topological representation of stereoisomerism. I. Polytopal rearrangements. *J. Am. Chem. Soc.* **1969**, *91*, 1636−1643. (b) Muetterties, E. Topological representation of stereoisomerism. II. The five-atom family. *J. Am. Chem. Soc.* **1969**, *91*, 4115−4122.
(28) (a) Gillespie, R. J.; Nyholm, R. S. Inorganic stereochemistry. *Q. Rev., Chem. Soc.* **1957**, *11*, 339−380. (b) Gillespie, R. J. Fifty years of the VSEPR model. *Coord. Chem. Rev.* **2008**, *252*, 1315−1327. (c) Bartell, L. S.; Plato, V. Gillespie-Nyholm aspects of force fields. I. Points-on-a-sphere and extended Hueckel molecular orbital analyses of trigonal bipyramids. *J. Am. Chem. Soc.* **1973**, *95*, 3097−3104. (d) Dashevskii, V. G.; Asatryan, R.; Baranov, A. P. Interligand interaction and three-dimensional structure of coordination compounds. Compounds of the tris(bidentate)M type. *J. Struct. Chem.* **1979**, *19*, 678−686.
(29) (a) Berry, R. S. Correlation of Rates of Intramolecular Tunneling Processes, with Application to Some Group V Compounds. *J. Chem. Phys.* **1960**, *32*, 933−938. (b) Berry, R. S. Time-Dependent Measurements and Molecular Structure: Ozone. *Rev. Mod. Phys.* **1960**, *32*, 447−454.
(30) Bürgi, H. B.; Dunitz, J. D. From crystal statics to chemical dynamics. *Acc. Chem. Res.* **1983**, *16*, 153−161.
(31) Cahoon, J. F.; Sawyer, K. R.; Schlegel, J. P.; Harris, C. B. Determining Transition-State Geometries in Liquids Using 2D-IR. *Science* **2008**, *319*, 1820−1823.
(32) Wernet, P.; Kunnus, K.; Josefsson, I.; Rajkovic, I.; Quevedo, W.; Beye, M.; Schreck, S.; Grübel, S.; Scholz, M.; Nordlund, D.; Zhang, W.; Hartsock, R. W.; Schlotter, W. F.; Turner, J. J.; Kennedy, B.; Hennigs, F.; De Groot, F. M. F.; Gaffney, K. J.; Techert, S.; Odelius, M.; Föhlisch, A. Orbital-specific mapping of the ligand exchange dynamics of $Fe(CO)_5$ in solution. *Nature* **2015**, *520*, 78−81.
(33) Whitesides, G. M.; Mitchell, H. L. Pseudorotation in tetrafluorodimethylaminophosphorane. *J. Am. Chem. Soc.* **1969**, *91*, 5384−5386.
(34) Ugi, I.; Marquarding, D.; Klusacek, H.; Gillespie, P.; Ramirez, F. Berry pseudorotation and turnstile rotation. *Acc. Chem. Res.* **1971**, *4*, 288−296.
(35) Gillespie, P.; Hoffman, P.; Klusacek, H.; Marquarding, D.; Pfohl, S.; Ramirez, F.; Tsolis, E. A.; Ugi, I. Non-rigid Molecular Skeletons—Berry Pseudorotation and Turnstile Rotation. *Angew. Chem., Int. Ed. Engl.* **1971**, *10*, 687−715.
(36) Russegger, P.; Brickmann, J. Brickmann, Pseudorotation of trigonal bipyramidal molecules: Berry rotation contra"“" ""turnstile"“" rotation in PF_5. *Chem. Phys. Lett.* **1975**, *30*, 276−278.
(37) Altmann, J. A.; Yates, K.; Csizmadia, I. G. Intramolecular ligand exchange in phosphoranes. A comparison of Berry pseudorotation and turnstile rotation. *J. Am. Chem. Soc.* **1976**, *98*, 1450−1454.
(38) Jesson, J. P.; Muetterties, E. L. Dynamic Molecular Processes in Inorganic and Organometallic Compounds. In *Dynamic Nuclear Magnetic Resonance Spectroscopy*; Jackman, L. M., Cotton, F. A., Eds.; Academic Press: New York, 1975; pp 253−316.

https://dx.doi.org/10.1021/acs.inorgchem.0c01708
Inorg. Chem. 2020, 59, 11757−11769

(39) (a) Ugi, I.; Marquarding, D.; Klusacek, H.; Gokel, G.; Gillespie, P. Chemistry and Logical Structures. *Angew. Chem.* **1970**, *82*, 741−771. (b) Ramirez, F.; Ugi, I.; Lin, F.; Pfohl, S.; Hoffman, P.; Marquarding, D. Permutational Isomerization of Caged Polycyclic Oxyphosphoranes. *Tetrahedron* **1974**, *30*, 371−376.

(40) (a) Kutzelnigg, W.; Wasilewski, J. Theoretical study of the reaction PH_5 PH_3+ + H_2. *J. Am. Chem. Soc.* **1982**, *104*, 953−960. (b) Bento, A. P.; Bickelhaupt, F. M. Frontside versus Backside S(N)2 substitution at group 14 atoms: origin of reaction barriers and reasons for their absence. *Chem. - Asian J.* **2008**, *3*, 1783−1792.

(41) (a) Musher, J. I.; Agosta, W. C. Modes of rearrangement in substituted octahedral complexes. *J. Am. Chem. Soc.* **1974**, *96*, 1320−1325. (b) Muetterties, E.; Guggenberger, L. J. Idealized polytopal forms. Description of real molecules referenced to idealized polygons or polyhedra in geometric reaction path form. *J. Am. Chem. Soc.* **1974**, *96*, 1748−1756.

(42) (a) Torker, S.; Khan, R. K. M.; Hoveyda, A. H. J. The Influence of Anionic Ligands on Stereoisomerism of Ru Carbenes and Their Importance to Efficiency and Selectivity of Catalytic Olefin Metathesis Reactions. *J. Am. Chem. Soc.* **2014**, *136*, 3439−3455. (b) Mikus, M. S.; Torker, S.; Xu, C. X.; Li, B.; Hoveyda, A. H. Pentacoordinate Ruthenium(II) Catecholthiolate and Mercaptophenolate Catalysts for Olefin Metathesis: Anionic Ligand Exchange and Ease of Initiation. *Organometallics* **2016**, *35*, 3878−3892. (c) Chen, P. Designing Sequence Selectivity into a Ring-Opening Metathesis Polymerization Catalyst. *Acc. Chem. Res.* **2016**, *49*, 1052−1060.

(43) (a) Balch, A. L.; Miller. 1,2-Dithiolene Complexes of Ruthenium and Iron. *Inorg. Chem.* **1971**, *10*, 1410−1415. (b) Bernal, I.; Clearfield, A.; Epstein, E. F.; Ricci, J. S.; Balch, A. L.; Miller, J. J. Isomeric conformations in a pentaco-ordinated ruthenium compound; crystal and molecular structures of the orange and violet isomers of $(Ph_3P)_2[(CF_3)_2C_2S_2]Ru(CO)$. *J. Chem. Soc., Chem. Commun.* **1973**, *2*, 39−40. (c) Bernal, I.; Clearfield, A.; Ricci, J. S. Crystal structure of the orange isomer of $[(C_6H_5)_3P]_2[C_2S_2(CF_3)_2]RuCO$. *J. Cryst. Mol. Struct.* **1974**, *4*, 43−54. (d) Clearfield, A.; Epstein, E. F.; Bernal, I. J. The crystal and molecular structure of the violet isomer of $(_3P)_2[(CF_3)_2C_2S_2]$-RuCO. *J. Coord. Chem.* **1977**, *6*, 227−240.

(44) (a) Porter, T. M.; Wang, J.; Li, Y.; Xiang, B.; Salsman, C.; Miller, J. S.; Xiong, W.; Kubiak, C. P. Direct observation of the intermediate in an ultrafast isomerization. *Chem. Sci.* **2019**, *10*, 113−117. (b) Porter, T. M.; Ostericher, A. L.; Kubiak, C. P. Steric and electronic control of an ultrafast isomerization. *Chem. Sci.* **2019**, *10*, 7907−7912.

(45) (a) Cahn, R. S.; Ingold, C.; Prelog, V. Specification of Molecular Chirality. *Angew. Chem., Int. Ed. Engl.* **1966**, *5*, 385−415. (b) Brown, J. M.; Mertis, K. Incipient chirality in organometallic triphenylphosphine derivatives. *J. Organomet. Chem.* **1973**, *47*, C5. (c) Costello, J. F.; Davies, S. G.; Gould, E. T. F.; Thomson, J. E. Conformational analysis of triphenylphosphine ligands in stereogenic monometallic complexes: tools for predicting the preferred configuration of the triphenylphosphine rotor. *Dalton Trans.* **2015**, *44*, 5451−5466.

(46) Frisch, M. J.; Trucks, G. W.; Schlegel, H. B.; Scuseria, G. E.; Robb, M. A.; Cheeseman, J. R.; Scalmani, G.; Barone, V.; Mennucci, B.; Petersson, G. A.; Nakatsuji, H.; Caricato, M.; Li, X.; Hratchian, H. P.; Izmaylov, A. F.; Bloino, J.; Zheng, G.; Sonnenberg, J. L.; Hada, M.; Ehara, M.; Toyota, K.; Fukuda, R.; Hasegawa, J.; Ishida, M.; Nakajima, T.; Honda, Y.; Kitao, O.; Nakai, H.; Vreven, T.; Montgomery, J. A., Jr.; Peralta, J. E.; Ogliaro, F.; Bearpark, M.; Heyd, J. J.; Brothers, E.; Kudin, K. N.; Staroverov, V. N.; Kobayashi, R.; Normand, J.; Raghavachari, K.; Rendell, A.; Burant, J. C.; Iyengar, S. S; Tomasi, J.; Cossi, M.; Rega, N.; Millam, J. M.; Klene, M.; Knox, J. E.; Cross, J. B.; Bakken, V.; Adamo, C.; Jaramillo, J.; Gomperts, R.; Stratmann, R. E.; Yazyev, O.; Austin, A. J.; Cammi, R.; Pomelli, C.; Ochterski, J. W.; Martin, R. L.; Morokuma, K.; Zakrzewski, V. G.; Voth, G. A.; Salvador, P.; Dannenberg, J. J.; Dapprich, S.; Daniels, A. D.; Farkas, O.; Foresman, J. B.; Ortiz, J. V.; Cioslowski, J.; Fox, D. J. *Gaussian 09, Revision D.01*; Gaussian, Inc.: Wallingford, CT, 2013.

(47) Becke, A. D. J. Density-functional thermochemistry. III. The role of exact exchange. *J. Chem. Phys.* **1993**, *98*, 5648−5652.

(48) (a) Becke, A. D. Density-functional exchange-energy approximation with correct asymptotic behavior. *Phys. Rev. A: At., Mol., Opt. Phys.* **1988**, *38*, 3098−3100. (b) Lee, C.; Yang, W.; Parr, R. G. Development of the Colle-Salvetti correlation-energy formula into a functional of the electron density. *Phys. Rev. B: Condens. Matter Mater. Phys.* **1988**, *37*, 785−789. (c) Perdew, J. P. Density-functional approximation for the correlation energy of the inhomogeneous electron gas. *Phys. Rev. B: Condens. Matter Mater. Phys.* **1986**, *33*, 8822−8824.

(49) Tao, J.; Perdew, J. P.; Staroverov, V. N.; Scuseria, G. E. Climbing the Density Functional Ladder: Nonempirical Meta−Generalized Gradient Approximation Designed for Molecules and Solids. *Phys. Rev. Lett.* **2003**, *91*, 146401.

(50) Chai, J.-D.; Head-Gordon, M. Long-range corrected hybrid density functionals with damped atom−atom dispersion corrections. *Phys. Chem. Chem. Phys.* **2008**, *10*, 6615−6620.

(51) Zhao, Y.; Truhlar, D. G. J. A new local density functional for main-group thermochemistry, transition metal bonding, thermochemical kinetics, and noncovalent interactions. *J. Chem. Phys.* **2006**, *125*, 194101.

(52) Zhao, Y.; Truhlar, D. G. The M06 suite of density functionals for main group thermochemistry, thermochemical kinetics, noncovalent interactions, excited states, and transition elements: two new functionals and systematic testing of four M06-class functionals and 12 other functionals. *Theor. Chem. Acc.* **2008**, *120*, 215−241.

(53) (a) Grimme, S.; Antony, J.; Ehrlich, S.; Krieg, H. J. A consistent and accurate ab initio parametrization of density functional dispersion correction (DFT-D) for the 94 elements H-Pu. *J. Chem. Phys.* **2010**, *132*, 154104. (b) Goerigk, L.; Grimme, S. J. Efficient and Accurate Double-Hybrid-Meta-GGA Density Functionals—Evaluation with the Extended GMTKN30 Database for General Main Group Thermochemistry, Kinetics, and Noncovalent Interactions. *J. Chem. Theory Comput.* **2011**, *7*, 291−309.

(54) Weigend, F.; Ahlrichs, R. Balanced basis sets of split valence, triple-ζ valence and quadruple-ζ valence quality for H to Rn: Design and assessment of accuracy. *Phys. Chem. Chem. Phys.* **2005**, *7*, 3297−3305.

(55) Fukui, K. The path of chemical reactions - the IRC approach. *Acc. Chem. Res.* **1981**, *14*, 363−368.

(56) Weigend, F.; Häser, M.; Patzelt, H.; Ahlrichs, R. RI-MP2: Optimized auxiliary basis sets and demonstration of efficiency. *Chem. Phys. Lett.* **1998**, *294*, 143.

(57) Marenich, A. V.; Cramer, C. J.; Truhlar, D. G. J. Universal Solvation Model Based on Solute Electron Density and on a Continuum Model of the Solvent Defined by the Bulk Dielectric Constant and Atomic Surface Tensions. *J. Phys. Chem. B* **2009**, *113*, 6378−6396.

(58) Addison, A. W.; Rao, T. N.; Reedijk, J.; van Rijn, J.; Verschoor, G. C. Synthesis, Structure, and Spectroscopic Properties of Copper(II) Compounds containing Nitrogen-Sulphur Donor Ligands; the Crystal and Molecular Structure of Aqua[1,7-bis(N-methylbenzimidazol-2′-yl)-2,6-dithiaheptane]copper(II) Perchlorate Continuous symmetry measures of penta-coordinate molecules: Berry and non-Berry distortions of the trigonal bipyramid. *J. Chem. Soc., Dalton Trans.* **1984**, 1349−1356.

(59) (a) Lim, B. S.; Fomitchev, D. V.; Holm, R. H. Nickel Dithiolenes Revisited: Structures and Electron Distribution from Density Functional Theory for the Three-Member Electron-Transfer Series $[Ni(S_2C_2Me_2)_2]$0,1-,2-. *Inorg. Chem.* **2001**, *40*, 4257−4262. (b) Eisenberg, R.; Gray, H. B. Noninnocence in Metal Complexes: A Dithiolene Dawn. *Inorg. Chem.* **2011**, *50*, 9741−9751. (c) Tang, H.; Guan, J.; Hall, M. B. Understanding the Radical Nature of an Oxidized Ruthenium Tris(thiolate) Complex and Its Role in the Chemistry. *J. Am. Chem. Soc.* **2015**, *137*, 15616−15619. (d) Tang, H.; Brothers, E. N.; Hall, M. B. The Distinctive Electronic Structures of Rhenium Tris(thiolate) Complexes, an Unexpected Contrast to the Valence Isoelectronic Ruthenium Tris(thiolate) Complexes. *Inorg. Chem.* **2017**, *56*, 583−593. (e) Tang, H.; Brothers, E. N.; Grapperhaus, C. A.; Hall, M. B. Electrocatalytic Hydrogen Evolution and Oxidation with Rhenium

https://dx.doi.org/10.1021/acs.inorgchem.0c01708
Inorg. Chem. 2020, 59, 11757−11769

Tris(thiolate) Complexes: A Competition between Rhenium and Sulfur for Electrons and Protons. *ACS Catal.* **2020**, *10*, 3778−3789.
(60) (a) Darensbourg, M. Y. *Progress in Inorganic Chemistry: Ion Pairing Effects on Transition Metal Carbonyl Anions*; Wiley−Interscience: New York, 1985; Vol. 33, p 239. (b) Darensbourg, M. Y.; Hanckel, J. M. The Use of Ion-pairing Phenomena in the Assignment of (CO) IR Bands of $PV(CO)_5^-$. *J. Organomet. Chem.* **1981**, *217*, C9−C13. (c) Darensbourg, M. Y.; Hanckel, J. M. Site-Specific Ion Pairing of Monosubstituted Vanadium Carbonylates, $LV(CO)_5^-$. *Organometallics* **1982**, *1*, 82−87.

https://dx.doi.org/10.1021/acs.inorgchem.0c01708
Inorg. Chem. 2020, 59, 11757−11769